A Cognitive Sub-Nyquist MIMO Radar Prototype

KUMAR VIJAY MISHRA ⓘ
The University of Iowa, Iowa City USA

YONINA C. ELDAR
Weizmann Institute of Science, Rehovot, Israel

ELI SHOSHAN
MOSHE NAMER
MAXIM MELTSIN
Technion-Israel Institute of Technology, Haifa, Israel

We present a cognitive prototype that demonstrates a colocated, frequency-division-multiplexed, multiple-input multiple-output (MIMO) radar, which implements both temporal and spatial sub-Nyquist sampling. The signal is sampled and recovered via the Xampling framework. Cognition is due to the fact that the transmitter adapts its signal spectrum by emitting only those subbands that the receiver samples and processes. Real-time experiments demonstrate sub-Nyquist MIMO recovery of target scenes with 87.5% spatio-temporal bandwidth reduction and signal-to-noise-ratio of −10 dB.

I. INTRODUCTION

Multiple-input-multiple-output (MIMO) radar has been the topic of extensive research during the past decade [1]–[3]. This is largely because MIMO offers capabilities that outweigh an equivalent, standard phased array radar such as finer angular resolution [4], spatial diversity [5], adaptive array realization [6], [7], and enhanced parameter identifiability [8]. Similar to a standard phased-array radar, MIMO uses an array of several transmit (Tx) and receive (Rx) antenna elements. However, while a phased array transmits scaled versions of a single waveform, each of the MIMO radar transmitters may emit a different probing signal. The angular resolution of MIMO is equal to that of a *virtual* uniform linear array (ULA) with the same antenna aperture but many more antenna elements.

MIMO radars are usually classified as *widely separated* or *colocated* depending on the antenna placement. Widely separated MIMO antennas are located far from each other resulting in different radar cross sections (RCS) of the same target for each Tx–Rx antenna pair. This spatial diversity is advantageous in detection of a target with small backscatter and low speed [5], [9]. In a colocated MIMO radar [2], [10], the antenna elements are placed close to each other so that the RCS of a target appears identical to all the elements. The primary advantage of colocated MIMO is its high angular resolution [11] arising from its waveform diversity based on the mutual orthogonality—usually in time, frequency or code—of different transmit signals. A colocated MIMO receiver separates and coherently processes the target echoes corresponding to each transmitter in multiple Tx–Rx channels. In this paper, our focus is on colocated MIMO radar.

When considering a MIMO radar, the spatial Nyquist theorem implies that an antenna array must not admit less than two signal samples per spatial period of the incident wave [12]. The spatial period is the operating wavelength λ of the radar. Otherwise, *spatial aliasing* is introduced leading to multiple beams in the antenna pattern, thereby reducing its directivity. In order to achieve high angular resolution, this implies a large virtual aperture with several elements that are located at least $\lambda/2$ spacing from each other. In sampling terms, the $\lambda/2$ ULA and the MIMO virtual ULA perform spatial sampling at the Nyquist rate. Even though a MIMO radar has less elements than an equivalent virtual phased array, it must employ multiple Tx–Rx chains resulting in huge hardware cost and very large computational complexity [13]. The range-time resolution of the radar is improved by transmitting signals with large bandwidth, which necessitate large sampling rates leading to high energy consumption and additional cost of high-rate analog-to-digital converters (ADCs). When the MIMO transmit signals use waveform orthogonality based on frequency, the combined transmit spectrum may be excessively wider than conventional radars.

Several methods have been proposed to address the problem of reducing the abovementioned costs on hardware, energy, and area in conventional MIMO radars (see

e.g. [14]–[16] for a review). Most exploit the fact that the target scene is *sparse* facilitating the use of compressed sensing (CS) methods [12], [17]. Early works on CS-based MIMO radars focused on reducing only the temporal sampling rate in distributed [18] and colocated configurations [19], [20], including passive arrays [21]. In [22]–[24], the received signal samples from an array radar are processed as data matrices which, under certain conditions, are low rank. Random sampling in the temporal domain results in a partially observed data matrix whose missing entries may be retrieved using matrix completion methods. The target parameters are then recovered through classic Nyquist radar signal processing. All the abovementioned applications of temporal CS still retain all antenna elements of a MIMO radar, thereby providing no reduction in the array hardware cost. Furthermore, while the receiver in these applications processes less measurements, the analog sampling with low-rate ADCs remains unexamined and CS-based target recovery procedures require dense sampling matrices.

Later works considered randomly reducing the number of antenna elements and employing CS-based target scene reconstruction [25], [26]. In [27], spatial compressed sensing for random MIMO arrays was proposed and performance guarantees for recovery were provided. This setup was extended to phased array and phased-MIMO hybrids in [28]. Other sparse arrays such as spatial coprime sampling for MIMO radars are suggested in [29]. A very recent work [30] combines random reduction in both antenna elements and transmit pulses. Each receiver in these sparse MIMO array methods samples at the Nyquist rate and, therefore, requires high signal bandwidth and high-rate ADCs.

Recently, Cohen *et al.* [31] proposed a *sub-Nyquist colocated MIMO radar* (or SUMMeR, hereafter) that can recover the target range and azimuth at native resolutions by simultaneously thinning an antenna array and sampling received signals at sub-Nyquist rates. The SUMMeR system was inspired by earlier works in [32] and [33], which described sub-Nyquist sampling in a single antenna radar and demonstrated it through a custom-built prototype. The recovery algorithm relies on modeling the received radar signal with finite degrees of freedom per unit of time or as a finite-rate-of-innovation (FRI) signal [12]. The *Xampling* framework is then used to obtain Fourier coefficients from the low-rate samples (or *Xamples*) of this FRI signal [12, p. 387–388] [33]. Application of Xampling in space and time enables sub-Nyquist sampling without loss of any of the aforementioned radar resolutions. The Xamples are expressed as a matrix of unknown target parameters and the reconstruction algorithm is derived by extending orthogonal matching pursuit [12] to simultaneously solve a system of CS matrix equations. A low-rate beamforming technique in the frequency domain called *Doppler focusing* [33] is added to the FRI-Xampling framework to also recover Doppler velocities along with delays and direction-of-arrival (DoA).

In SUMMeR, the radar antenna elements are randomly placed within the aperture, and signal orthogonality is achieved by frequency division multiplexing (FDM). In a conventional MIMO radar, the use of nonoverlapping FDM waveforms results in strong range-azimuth coupling [7], [34] in the receiver processing, and therefore, it is common to use orthogonal code signals (i.e., code division multiplexing). The coupling due to FDM can be reduced by randomizing either the carrier frequencies across transmitters [35] or the element locations in the aperture. Our sub-Nyquist MIMO prototype adopts the latter approach. It employs narrow individual transmit bandwidth for high azimuth resolution and large overall total bandwidth for high range resolution.

Here, we present a prototype that implements the SUMMeR concept in hardware by demonstrating sub-Nyquist sampling in both time and space in a real radar environment. Preliminary results of this paper appeared in our conference publications [36], [37]. In this paper, we extend the prototype to implement a *cognitive* MIMO radar. In recent years, cognitive radar has garnered considerable attention of the remote sensing community. The main advantage of such a system is its ability to learn the target environment and then adapt both the transmit and receive processing for optimal performance [38], [39]. Conventional radars can also optimize and change their processing techniques depending on the target scene, but their adaptability is restricted to receive processing only. Several possible radar cognition capabilities have been suggested where the environment specifications and corresponding suitable adaptive behaviors vary widely; examples include transmit beam scheduling based on previous tracking history of the targets [40], array adaptability and aperture sharing [41], and designing transmit waveform codes that avoid interfering bands by other licensed services [42]–[46].

In this paper, we consider cognitive radar in the latter context of spectrum sharing, which has also been recently explored between MIMO radar and MIMO communications [47]–[49]. Since the sub-Nyquist receiver samples and processes only a few disjoint subbands [43], [50], our cognitive SUMMeR (CoSUMMeR) prototype transmits only in these subbands, leaving the rest of the transmit spectrum to be used by other services. Such a radar not only avoids radio-frequency (RF) interference from other licensed radiators in the vacant nontransmit subbands but also disguises the transmit frequencies as an effective electronic counter measure. Limiting the signal transmission to selective subbands allows for more in-band power resulting in an increase in signal-to-noise ratio (SNR).

For a monostatic sub-Nyquist radar, [32] presented the hardware realization of temporal sub-Nyquist sampling in the radar through *multiband* sampling [51] in the receiver. Later, this prototype was extended to sub-Nyquist clutter removal in [52] and modified in [53] to demonstrate monostatic cognitive sub-Nyquist radar. In these implementations, a few randomly chosen, narrow subbands of the received signal spectrum are prefiltered before being sampled by low-rate ADCs. Since these implementations apply a bandpass filter and an ADC for each subband, a similar implementation of temporal sub-Nyquist sampling in each channel of a MIMO receiver would require

enormous hardware resources. As we explain in Section III, we circumvent such a design in CoSUMMeR by using the multiband version of foldable sampling as proposed in [51] and [54]. This approach can be implemented by a single low-rate ADC to sample all subbands simultaneously and leads to realization of a compact, hand-held prototype. We mitigate the consequent increase in the subsampling noise through use of analog preprocessing filters with high stop-band attenuation. Our design strategy enables configuring the prototype either as a filled or thinned array, thereby allowing comparison of Nyquist and sub-Nyquist spatial sampling using the same hardware.

Hardware implementations of MIMO radars in surveil-lance applications are not common [13] . But, due to their ubiquitous illumination, MIMO radars have been very popular as both narrow and wide-band imaging sensors for far-field targets in synthetic aperture radar (SAR) [55], [56], inverse SAR (ISAR) [57], and ultrawideband imaging [58]. Many MIMO imaging radar testbeds exist in X- [59]–[61], Ka- [62], and W-bands [63] for short-range applications such as environment monitoring, through-the-wall imaging, and automotive collision avoidance. The small size of antennas and other RF devices in these radar bands is helpful in building experimental testbeds. Very recently, miniature near-field MIMO imaging radar prototypes have been demonstrated [64], [65]. Inspired by these implementations, we chose an X-band operating frequency for CoSUMMeR signal and target models. Our first real-time proof-of-concept experimental results show that, compared to a Nyquist eight Tx $\times$ 10 Rx array, the CoSUMMeR array with four Tx and 5 Rx is capable of detecting targets up to SNR of -10 dB with spatial and temporal sampling rate reduction of 50% and 80%, respectively. The CoSUM-MeR design yields a combined spatio-temporal bandwidth reduction of 87.5% while also bringing down the number of hardware channels by 75%. Moreover, in low noise scenarios (~ -15 dB), CoSUMMeR shows better detection performance than the Nyquist array.

In the following section, we summarize the basic theory of our CoSUMMeR prototype. We evaluate the system requirements and formulate our design philosophy in Section III. A thorough description of the prototype is provided in Section IV, including all major submodules. We present results obtained by the prototype in real-time experiments in Section V and conclude in Section VI.

Throughout this paper, we reserve boldface lowercase, boldface uppercase, and calligraphic letters for vectors, matrices, and index sets, respectively. We denote the transpose and Hermitian by $(\cdot)^T$ and $(\cdot)^H$, respectively. The Kronecker product is written as $\otimes$. The notation tr $\{\cdot\}$ is the trace of the matrix, $|\cdot|$ is the determinant, and E $[\cdot]$ is the statistical expectation function. The function diag$(\cdot)$ outputs a diagonal matrix with the input vector along its main diagonal. The Fourier matrix $\mathbf{F}_N$ is a matrix of size $N \times N$ with (n, k)th entry given by $e^{\frac{-j2\pi nk}{N}}$. We use $\mathbf{I}_N$ for the identity matrix of size $N \times N$. Table I summarizes some of the important notations in this paper.

TABLE I
Glossary of Notations

Symbol	Description
T	Number of transmitters in a Nyquist MIMO array
R	Number of receivers in a Nyquist MIMO array
M	Number of transmitters in a sub-Nyquist MIMO array
Q	Number of receivers in a sub-Nyquist MIMO array
Z	Normalized aperture
ξ_m	Location of mth transmitter in SUMMeR array
ζ_q	Location of qth receiver in SUMMeR array
Z	Normalized aperture
λ	Operating wavelength
f_c	Common carrier frequency
c	Speed of light
$h_m(t)$	Non-cognitive time-domain pulse of mth transmitter
$\widetilde{h}_m(t)$	Cognitive time-domain pulse of mth transmitter
$H_m(\omega)$	CTFT of $h_m(t)$
$\widetilde{H}_m(\omega)$	CTFT of $\widetilde{h}_m(t)$
f_m	Center frequency of $h_m(t)$
T_p	Pulse width
τ	PRI
P_t	Total transmit power at each transmitter
L	Number of targets
R_l	Range of the lth target
τ_l ($\hat{\tau}_l$)	True (estimated) time delays of the lth target
α_l	Reflectivity of the lth target
v_l	Doppler velocity of the lth target
f_l^D ($\hat{f}_l^D$)	True (estimated) Doppler frequency of the lth target
θ_l	Azimuth angle of the lth target
ϑ_l ($\hat{\vartheta}_l$)	True (estimated) Azimuth parameter $\sin \theta_l$
β_{mq}	Array structure parameter
$x_q(t)$	Baseband receive signal at qth receiver
$x_q^p(t)$	Baseband receive signal at qth receiver for pth pulse
$y_{m,q}^p$	Fourier coefficients for mth channel, qth receiver, pth pulse
$\Phi_{m,q}^\nu$	Fourier coefficients $y_{m,q}^p$ after focusing at frequency ν
N	Number of Fourier coefficients in each channel
κ	Set of sampled Fourier coefficients per channel
K	Number of sampled Fourier coefficients per channel
$\mathbf{Z}^m$	All sampled Fourier coefficients for mth transmitter
$\mathbf{A}^m$	Range dictionary
$\mathbf{B}^m$	Azimuth dictionary
$\mathbf{F}_P$	Fourier matrix of size $P \times P$
$\mathbf{X}_D$	Sparse matrix with non-zero elements at target locations
B_h	Non-cognitive bandwidth of each transmitter
N_b	Number of sub-bands in each cognitive transmit pulse
$\mathcal{B}_i$	Set of frequencies in ith subband

II. BASIC THEORY OF CoSUMMeR

Except for the cognitive transmission, our CoSUMMeR prototype follows the signal model and algorithms suggested in [31], and hence, we only summarize them here. Let the operating wavelength of the radar be λ and the total number of transmit and receive elements in a standard colocated MIMO radar array be T and R, respectively. The classic MIMO approach adopts a virtual ULA structure, where the receive antennas spaced by $\frac{\lambda}{2}$ and transmit antennas spaced by $R\frac{\lambda}{2}$ form two ULAs (or vice versa). Here, the coherent processing of a total of TR channels in the receiver creates a virtual equivalent of a phased array with TR $\frac{\lambda}{2}$-spaced receivers and normalized aperture $Z = \frac{TR}{2}$. This standard array structure and the corresponding receiver virtual array are illustrated in Fig. 1(a) and (b) for $T = 5$ and $R = 4$.

Consider now a sub-Nyquist colocated MIMO radar system that has $M < T$ transmit and $Q < R$ receive antennas. The locations of these antennas are chosen uniformly at random within the aperture of the virtual array mentioned above, that is $\{\xi_m\}_{m=0}^{M1} \sim \mathcal{U}[0, Z]$ and $\{\zeta_q\}_{q=0}^{Q1} \sim \mathcal{U}[0, Z]$,
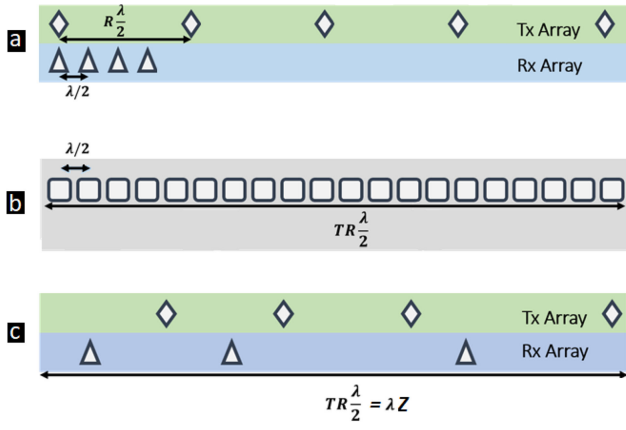
Fig. 1. Location of transmit (diamonds) and receive (triangles) antenna elements within the same physical aperture for (a) conventional MIMO array with $T = 5$ transmitters and $R = 4$ receivers, (b) virtual ULA with $TR = 20$ antenna elements, and (c) randomly thinned MIMO array with $M = 4$ transmitters and $Q = 3$ receivers.

respectively. An example can be seen in Fig. 1(c) with $M = 4$ and $Q = 3$. The mth transmitting antenna sends P pulses $s_m(t)$ given by

$$s_m(t) = \sum_{p=0}^{P-1} h_m(t - p\tau) e^{j2\pi f_c t}, \quad 0 \le t \le P\tau \quad (1)$$

where τ denotes the pulse repetition interval (PRI), $P\tau$ is the coherent processing interval (CPI), $f_c = c/\lambda$ is the common carrier frequency at the RF stage, c is the speed of light, and $\{h_m(t)\}_{m=0}^{M-1}$ is a set of narrowband, orthogonal FDM pulses centered at the modulating frequency f_m each with continuous-time Fourier transform (CTFT)

$$H_m(\omega) = \int_{-\infty}^{\infty} h_m(t) e^{-j\omega t} dt. \quad (2)$$

For simplicity, we assume that $f_c \tau$ is an integer, so that the delay $e^{-j2\pi f_c \tau p}$ is canceled in the modulation. The pulse time support is denoted by T_p.

Assume a target scene consisting of L nonfluctuating point targets following the Swerling-0 model [66] whose locations are given by their ranges R_l, Doppler velocity v_l, and azimuth angles θ_l, $1 \le l \le L$. The pulses transmitted by the radar are reflected back by the targets and collected at the receive antennas. When the received waveform is downconverted from RF to baseband, we obtain the following signal at the qth antenna

$$x_q(t) = \sum_{p=0}^{P-1} \sum_{m=0}^{M-1} \sum_{l=1}^{L} \alpha_l h_m (t - p\tau - \tau_l) e^{j2\pi \beta_{mq} \vartheta_l} e^{j2\pi f_l^D p\tau}$$
$$(3)$$

where α_l denotes the complex-valued reflectivity of the lth target, $\tau_l = 2R_l/c$ is the range-time delay the lth target, $f_l^D = \frac{2v_l}{c} f_c$ is the frequency in the Doppler spectrum, $\vartheta_l = \sin \theta_l$ is the azimuth parameter, and $\beta_{mq} = (\zeta_q + \xi_m)(f_m \frac{\lambda}{c} + 1)$ is governed by the array structure. For

processing, we express $x_q(t)$ as a sum of single frames

$$x_q(t) = \sum_{p=0}^{P-1} x_q^p(t) \quad (4)$$

where

$$x_q^p(t) = \sum_{m=0}^{M-1} \sum_{l=1}^{L} \alpha_l h(t - \tau_l - p\tau) e^{j2\pi \beta_{mq} \vartheta_l} e^{j2\pi f_l^D p\tau}. \quad (5)$$

The radar goal is to estimate the time delay τ_l, azimuth θ_l, and Doppler shifts f_l^D of each target from low rate samples of $x_q(t)$, and a small number of M channels and Q antennas.

A. Xampling in Time and Space

The application of Xampling in both space and time enables recovery of range, direction, and velocity at sub-Nyquist rates [31]. The sampling technique is the same as in temporal sub-Nyquist radar [33], except that now the low-rate samples are obtained in both range and azimuth domains.

The received signal $x_q(t)$ is separated into M channels, aligned, and normalized. The Fourier coefficients of the received signal corresponding to the channel that processes the mth transmitter echo at the qth receiver are

$$y_{m,q}^p[k] = \sum_{l=1}^{L} \alpha_l e^{j2\pi \beta_{mq} \vartheta_l} e^{-j\frac{2\pi}{\tau}k\tau_l} e^{-j2\pi f_m \tau_l} e^{j2\pi f_l^D p\tau} \quad (6)$$

where $-\frac{N}{2} \le k \le -\frac{N}{2} - 1$, f_m is the (baseband) carrier frequency of the mth transmitter and N is the number of Fourier coefficients per channel. Xampling obtains a set κ of arbitrarily chosen Fourier coefficients from low rate samples of the received channel signal such that $|\kappa| = K < N$.

As in traditional MIMO, assume that the time delays, azimuths, and Doppler frequencies are aligned to a grid. In particular, $\tau_l = \frac{\tau}{TN}s_l$, $\vartheta_l = -1 + \frac{2}{TR}r_l$, and $f_l^D = -\frac{1}{2\tau} + \frac{1}{P\tau}u_l$, where s_l, r_l, and u_l are integers satisfying $0 \le s_l \le TN - 1$, $0 \le r_l \le TR - 1$, and $0 \le u_l \le P - 1$, respectively.

Let $\mathbf{Z}^m$ be the $KQ \times P$ matrix with qth column given by the vertical concatenation of $y_{m,q}^p[k]$, $k \in \kappa$, for $0 \le q \le Q - 1$. We can then write $\mathbf{Z}^m$ as

$$\mathbf{Z}^m = (\mathbf{B}^m \otimes \mathbf{A}^m) \mathbf{X}_D \mathbf{F}_P^H. \quad (7)$$

Here, $\mathbf{A}^m$ denotes the $K \times TN$ matrix whose (k, n)th element is $e^{-j\frac{2\pi}{TN}\kappa_k n} e^{-j2\pi \frac{f_m}{B_h} \frac{n}{T}}$ with κ_k the kth element in κ, $\mathbf{B}^m$ is the $Q \times TR$ matrix with (q, p)th element $e^{-j2\pi \beta_{mq}(-1+\frac{2}{TR}p)}$, and $\mathbf{F}_P$ denotes the $P \times P$ Fourier matrix. The matrix $\mathbf{X}_D$ is a $T^2 NR \times P$ sparse matrix that contains the values α_l at the L indices $(r_l TN + s_l, u_l)$. The temporal, spatial, and frequency resolutions stipulated by $\mathbf{X}_D$ are $\frac{1}{TB_{B_h}}$, $\frac{2}{TR}$, and $\frac{1}{P\tau}$, respectively. The range and azimuth dictionaries $\mathbf{A}^m$ and $\mathbf{B}^m$ are not square matrices due to the low-rate sampling of Fourier coefficients at each receiver and reduction in antenna elements, respectively.

Therefore, the system of equations in (7) is undetermined in azimuth and range.

The minimum required number of SUMMeR transmit and receive elements as well as samples K to recover $\mathbf{X}_D$ depend only on the number of targets present as stated by Theorem 1. These design resources are, therefore, substantially fewer than the requirements of a Nyquist MIMO array.

THEOREM 1 ([31]) The minimal number of transmit and receive array elements, i.e., M and Q, respectively, required for perfect recovery of $\mathbf{X}_D$ with L targets in a noiseless setting are determined by $MQ \geq 2L$. In addition, the number of samples per receiver is at least $MK \geq 2L$ where K is the number of Fourier coefficients sampled per receiver and the number of pulses per transmitter is $P \geq 2L$.

B. Range-Azimuth-Doppler Recovery

To jointly recover the range, azimuth, and Doppler frequencies of the targets, Doppler focusing [33] is used in SUMMeR which, for a specific frequency v, yields

$$
\Phi^v_{m,q}[k] = \sum_{p=0}^{P-1} y^p_{m,q}[k] e^{-j2\pi v p \tau}
$$

$$
= \sum_{l=1}^{L} \alpha_l e^{j2\pi\beta_{mq}\vartheta_l} e^{-j\frac{2\pi}{\tau}(k+f_m\tau)\tau_l} \sum_{p=0}^{P-1} e^{j2\pi(f_l^D - v)p\tau}
$$

(8)

for $-\frac{N}{2} \leq k \leq -\frac{N}{2} - 1$. Since

$$
\sum_{p=0}^{P-1} e^{j2\pi(f_l^D - v)p\tau} \cong \begin{cases} P, & |f_l^D - v| < \frac{1}{2P\tau} \\ 0, & \text{otherwise} \end{cases}
$$

(9)

for each focused frequency v, (8) reduces to a two-dimensional problem, which can be solved using CS recovery techniques. We refer the reader to [31] for full details of this recovery algorithm. Note that Doppler focusing can be efficiently performed using the fast Fourier transform. Once $\mathbf{X}_D$ is recovered, the delays, azimuths, and Dopplers are, respectively, estimated as

$$
\hat{\tau}_l = \frac{\tau \Lambda_L(l, 1)}{TN},
$$

$$
\hat{\vartheta}_l = -1 + \frac{2\Lambda_L(l, 2)}{TR}, \text{ and } \hat{f}_l^D = -\frac{1}{2\tau} + \frac{\Lambda_L(l, 3)}{P\tau}
$$

(10)

where $\Lambda_t(l, i)$ is the (l, i)th element in the index set Λ_t at the tth iteration of the recovery algorithm. Since in real scenarios, target delays, Dopplers and azimuths are not necessarily aligned to a grid, a finer grid can be used around detection points on the coarse grid to reduce quantization error.

C. Cognitive SUMMeR

So far, we focused on processing the received signal in sub-Nyquist MIMO radar. The receiver design in the sub-Nyquist framework can be exploited to also alter the behavior of the radar transmitter. Let us assume that
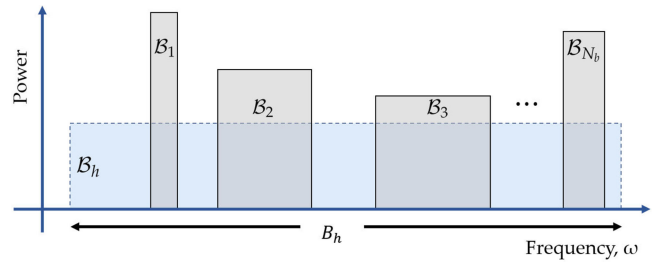

Fig. 2. Spectrum of a single transmit signal of a conventional radar uses the full bandwidth $\mathcal{B}_h$. A cognitive radar transmits only in subbands $\{\mathcal{B}_i\}_{i=1}^{N_b}$, but with more in-band power than the conventional radar.

$\mathcal{B}_h$ is the set of all frequencies in the single transmitter signal spectrum of effective bandwidth B_h. In cognitive radar transmission, the spectrum $\widetilde{H}_m(\omega)$ of each of the cognitive transmitted waveforms $\{\widetilde{h}_m(t)\}_{m=1}^M$ is limited to a total of N_b nonoverlapping frequency bands $\mathcal{B}_i$, $1 \leq i \leq N_b$ (see Fig. 2)

$$
\widetilde{H}_m(\omega) = \begin{cases} \gamma(\omega) H_m(\omega), & \omega \in \bigcup_{i=1}^{N_b} \mathcal{B}_i \subset \mathcal{B}_h \\ 0, & \text{otherwise} \end{cases}
$$

(11)

where $\gamma(\omega) = B_h/|\mathcal{B}_i|$ for $\omega \in \mathcal{B}_i$. The total transmit power P_t remains the same such that the power relation between the conventional and cognitive waveforms is

$$
\int_{-B_h/2}^{B_h/2} |H_m(\omega)|^2 \, d\omega = \sum_{i=1}^{N_b} \int_{\mathcal{B}_i} |\widetilde{H}_m(\omega)|^2 \, d\omega = P_t.
$$

(12)

In a cognitive radar, the sub-Nyquist receiver obtains the set κ of the Fourier coefficients only from the subbands $\mathcal{B}_i$. Note that a conventional radar that employs a Nyquist receiver will be unable to process echoes from disjoint subbands.

Cognitive transmission imparts two advantages to the CoSUMMeR hardware. First, as we explain in Section III-C, the spatial sub-Nyquist processing of large arrays can be easily designed without replicating the prefiltering operation for each subband in the hardware. Second, since the total transmit power remains the same, a cognitive signal has more in-band power resulting in an increase in SNR. For a monostatic cognitive sub-Nyquist radar, our earlier work [43] compares the performance of conventional and cognitive radars using the extended Ziv–Zakai lower bound (EZB) for the particular case of time delay estimation of a single target. As noted in [43], the SNR threshold for asymptotic performance of EZB in cognitive radar is lower than that of a conventional radar. When the noise increases and power remains constant for both radars, the asymptotic performance of cognitive radar EZB is more tolerant to noise. In this context, experimental results presented later in Section V provide a proof-of-concept of the theoretical intuition that CoSUMMeR performs better than noncognitive Nyquist and sub-Nyquist MIMO radars in low SNR scenarios.
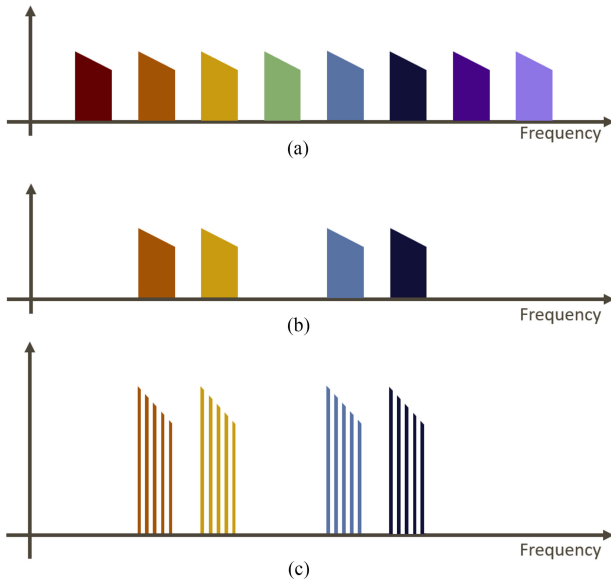
Fig. 3. Illustration of the one-sided transmit spectrum of (a) FDM-based conventional (spatial Nyquist) MIMO radar employing $T = 8$ transmitters, (b) SUMMeR with $M = 4$ transmitters, and (c) CoSUMMeR with each transmit signal restricted to only a few subbands but with more in-band power than SUMMeR.

Since the waveform orthogonality of transmit waveforms in SUMMeR is based on FDM, spatial compression through random removal of antenna elements in the transmit array also eliminates spectrum usage by those transmitters, as we illustrate in Fig. 3. The spectrum savings are further improved in CoSUMMeR through use of a small portion of the available bandwidth of the SUMMeR signal; the range resolution is not lost while sampling at a low rate.

In a spectrally crowded operational environment, the radar chooses its subband locations based on the interference levels at all available frequencies in the spectrum. In practice, a radar could obtain the spectral occupancy information through passive (receive only) sweeping across the desired spectrum. Spectral coexistence comprises some exchange of information between the radar and a coexisting communications system where the latter conveys the location of its signals to the radar. During the cognitive operation, equipped with the information from the communications system and passive sensing, the objective of the radar is to identify an appropriate transmit frequency set such that the radar's probability of detection P_d is maximized. For a fixed probability of false alarm P_{fa}, the P_d increases with higher signal-to-interference-and-noise-ratio (SINR). Hence, the frequency selection criterion is to choose subbands so that the SINR is maximized at the receiver. Our previous work [44] maps the cognitive subband selection problem to seeking a block-sparse vector and solves it by employing a structured greedy algorithm. This process is repeated every few scans.

III. DESIGN PHILOSOPHY

We now discuss the various design considerations for our CoSUMMeR prototype with the goal of designing a compact, portable system that demonstrates theoretical concepts of CoSUMMeR in practice.

A. Experimental Environment

The spatial and temporal sampling aspects of the sub-Nyquist MIMO prototype manifest only in the receiver processing. Therefore, we do not physically radiate the transmit waveforms from an antenna. Instead, we employ National Instruments AWR software design environment, which is capable of simulating complex sensing scenes including multiple targets, their ranges, Doppler velocities, RCS, and propagation losses in the medium. The AWR, therefore, provides reflected signals from the targets as received at the antenna waveguide front and is capable of modeling an RF receiver response with realistic component-level simulations. It outputs the demodulated signal at the intermediate-frequency (IF) stage of the analog receiver. We record the AWR output of the received signal at baseband for multiple transmit waveforms and target scenarios. The complex samples (in-phase $\mathcal{I}$ and quadrature-phase $\mathcal{Q}$ pairs) of the received signal are then stored in an on-board memory of a custom-designed waveform generator board. The prototype processes these prerecorded signals in real time. We omit the implementation of the up conversion to the RF carrier frequency in the transmitter and the corresponding down conversion in the receiver from this prototype. For reasons explained in Section I, we assume that the physical array aperture and simulated target response correspond to an X-band ($f_c = 10$ GHz) radar.

B. Spatial Sub-Nyquist Sampling

We consider the implementation of a MIMO radar architecture with resources that can handle eight Tx and ten Rx antenna elements. These elements can be positioned within a given physical aperture in several different constellations or *modes*. While operating at its maximum strength of eight Tx and ten Rx elements, the prototype can be programmed as a standard Nyquist array or ULA (Mode 1) with an equivalent aperture of an 8×10 virtual array at X-band, i.e., 1.2 m. In Mode 2, the prototype utilizes the same 8×10 elements as a random array within the physical aperture of 1.2 m. Note that the equivalent virtual aperture of this array may be wider than the Nyquist Mode 1.

For the sub-Nyquist array, the prototype offers two options. It can operate as a thinned 4×5 array (Mode 3) with the corresponding Nyquist array being Mode 1. In this constellation, the receive channels corresponding to the removed transmit elements are not processed by the digital receiver. Mode 3, hence, demonstrates spatial sub-Nyquist sampling. The prototype can process the received signals for the same target scenario in both Mode 1 and 3 to allow for a comparison between spatial Nyquist and sub-Nyquist sampling methods.

In the second spatial sub-Nyquist configuration, the prototype functions as a 8×10 thinned array (Mode 4) for which the equivalent Nyquist antenna is the virtual 20×20 array with an aperture of 6 m. However, in this case, with a
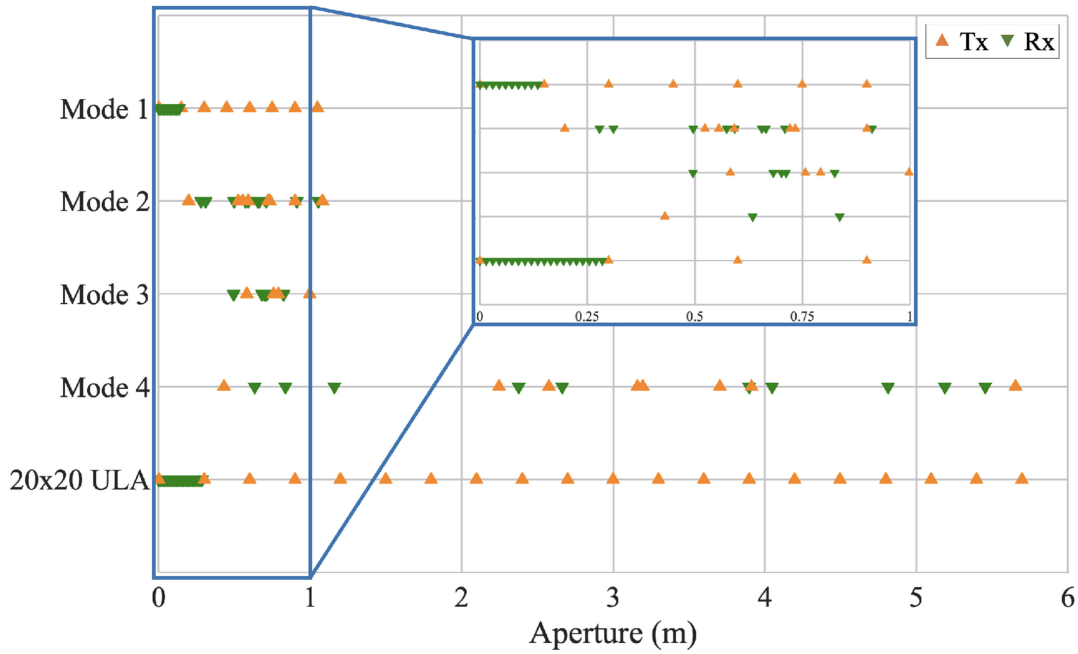
Fig. 4. Tx and Rx element locations for the hardware prototype modes over a 6 m antenna aperture. Mode 4's virtual array equivalent is the 20×20 ULA. The inset plot shows the selected region on a magnified scale.

resource limit of eight Tx and ten Rx, the prototype is unable to compare the Nyquist and sub-Nyquist arrays. Nonetheless, this provides an opportunity to evaluate sub-Nyquist processing at higher angular resolution than all other three modes. Fig. 4 shows exact details of element locations for all four modes.

In a random array, antenna selection may be decided through advanced methods, which optimize element placement for improved parameter estimation. These approaches include greedy search [30] or deep learning [41]. The random antenna placement in our prototype was determined through software simulations, which performed extensive search for optimum arrays. The random arrays that provided localization with minimum error for multiple targets were selected.

C. Temporal Sub-Nyquist Sampling

A conventional 8×10 MIMO radar receiver would require simultaneous hardware processing of 80 complex data streams (or 160 $\mathcal{I}$ and $\mathcal{Q}$ channels). A separate sub-Nyquist receiver for each of these 80 channels is expensive and increases the hardware size. Hence, we implement the eight channel analog processing chain for only one receive antenna element and then serialize the received signals of all ten elements through this chain. The analog processing chain consists of eight different filtering channels, which separate the received signal corresponding to each of the eight transmitters. This approach allows the prototype to implement a number of receivers even greater than ten because the eight-channel hardware places an upper limit on only the number of transmitters.

Given a particular receive element, we need to extract a set of Fourier coefficients κ, $|\kappa| = K$, (see Section II-A) from low rate samples of each of its transmit channels. It has been shown [17, pp. 210–268] that high recovery performance is attained when these coefficients are drawn uniformly at random. An ADC cannot, however, individually acquire each of the randomly chosen Fourier coefficients conveniently. Several practical implementations of sub-Nyquist receivers exist including the modulated wideband converter [67]. In particular, the sub-Nyquist radar prototype in [32] opted for *multiband sampling* where random disjoint subsets of κ are sampled, with each subset containing consecutive Fourier coefficients. This prototype used four random Fourier coefficient groups, prefiltered the baseband signal to corresponding four subbands (or Xampling *slices*), and sampled each subband through a separate low-rate ADC.

If we use the same prefiltering approach as in [32] for each of the eight channels of our sub-Nyquist MIMO prototype, then the hardware design would require a total of $4 \times 8 = 32$ bandpass filters (BPFs) and ADCs excluding the analog filters to separate transmit channels. Moreover, the hardware cost would increase dramatically if the number of subbands are increased or separate analog channels are implemented for each receiver. We sidestep this requirement by adopting cognitive transmission wherein the analog signal of each channel lives only in certain predetermined subbands and consequently, a BPF stage for each subband is not required.

More importantly, for each channel, a single low-rate ADC can *subsample* this narrow-band signal as long as the subbands are *coset* bands so that they do not alias after sampling. This is based on the *foldable sampling* suggested for ultrawideband reception in [54] where the received signal is sampled below the Nyquist rate resulting in folding

over or aliasing of the signal spectrum that exceeds the Nyquist sampling rate f_s of the ADC. The signal distortion due to aliasing is avoided by notching out those Fourier coefficients from the transmit signal that will alias over the low-frequency part of the sampled signal. In particular, assume that the entire received signal consisting of N Fourier coefficients is divided into q groups of K coefficients. If we subsample this signal at the rate f_s/q, then K coefficients of each group will alias over each other in the sampled signal. In [54], K Fourier coefficients are chosen randomly from any of the q groups and the remaining $q-1$ aliasing coefficients are notched out in the transmit signal.

In CoSUMMeR, we employ *foldable multiband sampling* proposed in [51] for a millimeter wave sub-Nyquist receiver. Here, instead of selecting each coefficient randomly from q groups, we choose N_b sets of consecutive coefficients from each group such that the total number of coefficients is still K. This implementation needs only eight low-rate ADCs, one per channel. Another advantage of this approach is flexibility of the prototype in selecting the Xampling *slices*. Unlike [32], the number and spectral locations of slices are not permanently fixed, and they can be changed (within the constraints of aliasing due to subsampling).

Foldable sampling methods suffer from SNR loss due to aliasing of out-band noise. Therefore, the analog front-end must employ filters to reduce undesired leakage of noise. The stop-band attenuation specification of these filters is determined as follows. Let us assume the front-end BPF reduces the out-of-band white noise with power spectral density N_0 to N_{sub} before the translation of the signal to a lower band. For a signal with IF f_{IF}, the subsampling factor is $q = f_{IF}/f_s$. This subsampling will raise the out-of-band noise power by $2q$ (one spectrum from the negative and another from the positive side) so that the total overlapped noise power density increases to $2q N_{sub}$. If the overlapped noise power $2q N_{sub}$ is less than the additive white noise power N_0, then the receiver performance remains essentially unaffected. Now, consider a band-limited signal with power spectral density P_s. Then, the SNR of the signal sampled at Nyquist rate is given by $SNR_{Nyq} = P_s/N_0$. On the other hand, the SNR of the subsampled signal is $SNR_{sub} = P_s/(N_0 + 2q N_{sub})$. The degradation of SNR in dB due to out-band noise is $SNR_{loss} = 10\log_{10}(SNR_{Nyq}/SNR_{sub}) = 10\log_{10}\left(1 + \frac{2q N_{sub}}{N_0}\right)$. As we show in Section IV-C, analog filters with reasonably high stop-band attenuation are sufficient to mitigate this SNR loss.

D. Cognitive Operation and Dynamic Range

Radar receivers typically have dynamic range of tens of dBs to enable detection of targets with a wide range of RCS. In CoSUMMeR, we have an additional constraint of enabling the cognitive operation of the prototype. Therefore, we want to design a prototype with wide dynamic range so that it can handle high in-band power levels. Although there are several techniques to increase the dynamic range

Parameters	Mode 1	Mode 2	Mode 3	Mode 4
#Tx, #Rx	8,10	8,10	4,5	8,10
Element placement	Uniform	Random	Random	Random
Equivalent aperture	8x10	8x10	8x10	20x20
Angular resolution (sine of DoA)	0.025	0.025	0.025	0.005
Range resolution	1.25 m			
Signal bandwidth per Tx	12 MHz (15 MHz including guard-bands)			
Pulse width	4.2 μs			
Carrier frequency	10 GHz			
Unambiguous range	15 km			
Unambiguous DoA	180° (from -90° to 90°)			
PRI	100 μs			
Pulses per CPI	10			
Unambiguous Doppler	from -75 m/s to 75 m/s			

of a digital receiver [68], [69], it is primarily decided by the choice of the ADC. Three ADC design parameters predominantly affect its dynamic range: its Nyquist sampling rate that is determined by the bandwidth of the analog signal to be sampled; number b of digitized bits which should be large to sample with low quantization errors; and the saturation level P_{sat} dBm under, which ADC operation is linear. The lower limit of the dynamic range (in dBm) of the receiver expressed at a given bandwidth (BW) (typically, 1 MHz) is given by

$$DR_{low} = P_{sat} - 20\log_{10}(2^b) - 10\log_{10}\left(\frac{f_s/2}{BW}\right) \quad (13)$$

$$= P_{sat} - 6.02b - 10\log_{10}\left(\frac{f_s/2}{BW}\right). \quad (14)$$

Unfortunately, numerous factors degrade the ADC's ideal performance resulting in a lower SNR value and higher effective noise figure value [69]. These errors are often represented by replacing b with the effective number of bits (E_{NoB}), which is much lower than b. When quantization noise is also taken into account, the lower limit of the dynamic range (in dBm) is given by

$$DR_{low} = P_{sat} - 1.76 - 6.02 E_{NoB} - 10\log_{10}\left(\frac{f_s/2}{BW}\right) \quad (15)$$

so that the dynamic range itself (in dB) is $DR = P_{sat} - DR_{low}$. Our design goal is to choose an ADC with high E_{NoB} so that the dynamic range of the receiver does not degrade with subsampling.

IV. SYSTEM ARCHITECTURE

Table II summarizes the technical parameters of our CoSUMMeR prototype for all four array configurations. The desired range and angular resolutions as well as maximum unambiguous range and Doppler velocity requirements are based on some of the common MIMO radars mentioned in Section I. Based on these specifications, we chose ten pulses per CPI with a PRI of 100 μs. Each transmit signal has an approximately flat spectrum, over the extent of 12 MHz (one-sided band). The waveforms are separated from each other by a 3 MHz guard band so that the total bandwidth occupied by all eight transmitters is 120 MHz.
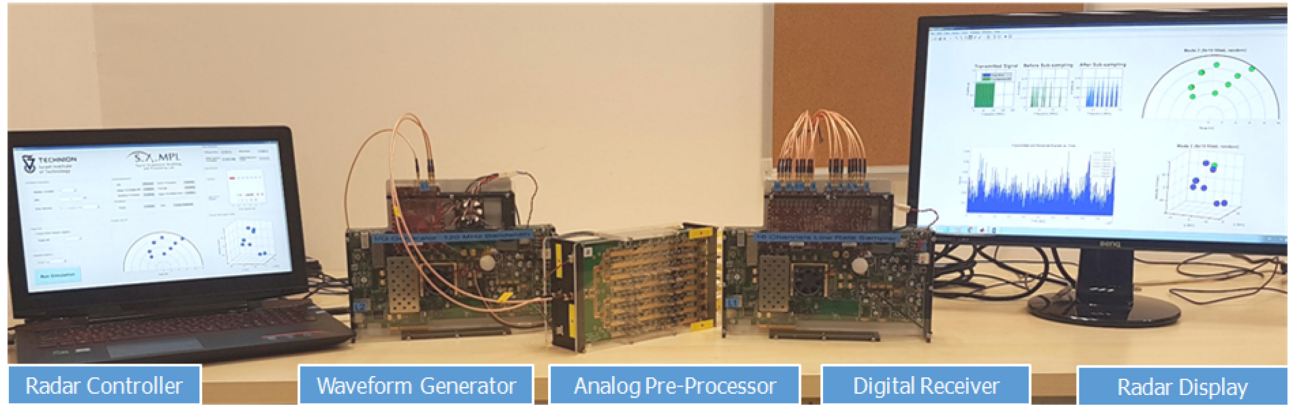
Fig. 5. CoSUMMeR prototype and its subsystems. The APP consists of two cards mounted on the opposite sides of a common chassis.
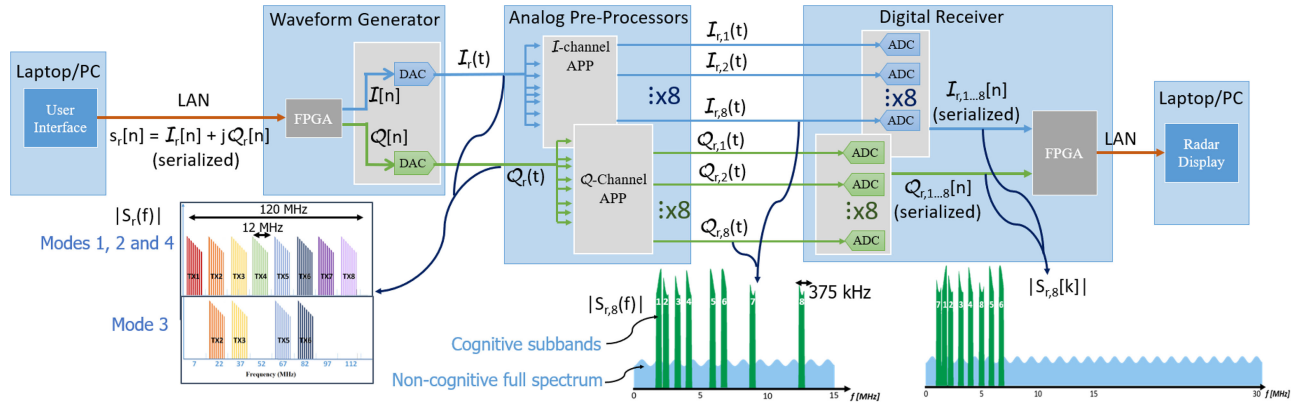

Fig. 6. Simplified block diagram of the CoSUMMeR prototype. The subscript r represents received signal samples for the rth receiver. Wherever applicable, the second subscript corresponds to a transmitter. The square brackets (parentheses) are used for digital (analog) signals. The spectrum $|S_r(f)|$ of the complex received signal for each mode over the 120 MHz frequency range before separating the echoes corresponding to individual transmitters is illustrated in the bottom left. The locations of cognitive subbands within the noncognitive full spectrum $|S_{r,8}(f)|$ for a Tx–Rx channel before subsampling is shown in the bottom middle. In the bottom right, the spectrum of the corresponding cognitive signal subsampled at 7.5 MHz is shown as $|S_{r,8}[k]|$ overlaid on the spectrum of the noncognitive signal sampled at the Nyquist rate of 30 MHz.

Fig. 5 shows the CoSUMMeR prototype. It consists of a radar controller, waveform generator, analog preprocessor (APP), digital receiver, and data-processor-combined-with-display. Fig. 6 illustrates the simplified block diagram of the prototype with the signal spectrum at every major stage. We now provide details on each one of the subsystems.

A. Radar Controller

The prototype is configured through the user interface of the radar controller software deployed on a high-end portable server. The software consists of two major components: waveform control and APP control. These components interact with each other and provide status to the data processor. The waveform control allows the user to select the target scenario, array constellations (or modes), and SNR levels of the received baseband signals. The option to operate Mode 3 cognitively is also provided, along with the facility to autocalibrate the prototype using built-in-test-equipment (BITE) and built-in-system-test signals [69]. The APP control allows the controller to skip individual Tx channels while operating in spatial sub-Nyquist mode. All hardware devices are individually powered and

the controller communicates with them over an Ethernet link.

B. Waveform Generator

The user selects the prototype mode from the control interface and passes the control triggers to the waveform generator card. The waveform generator is off-the-shelf Xilinx VC707 evaluation board that is custom fit with a 4DSP FMC204 16-bit DAC mezzanine card. The waveforms are stored as digital $\mathcal{I}/\mathcal{Q}$ pairs at baseband with a sample rate of 250 MHz for each channel. The transmit waveform is downloaded to the waveform generator's onboard 1 GB DDR3 memory via Ethernet interface either through a server or single-board computer. The field programmable gate array (FPGA) device then reads out the prestored waveform from the memory and employs 8 Gbps Serializer/Deserializer (SerDes) device to transfer it to two separate 16-bit DACs, one each for $\mathcal{I}$ and $\mathcal{Q}$ samples. The DACs then interpolate and convert the stored waveform to an analog baseband signal at a sample rate of 1 Gsps. This process continues until all the $\mathcal{I}$-$\mathcal{Q}$ pairs of received waveforms corresponding to each Tx–Rx chan-
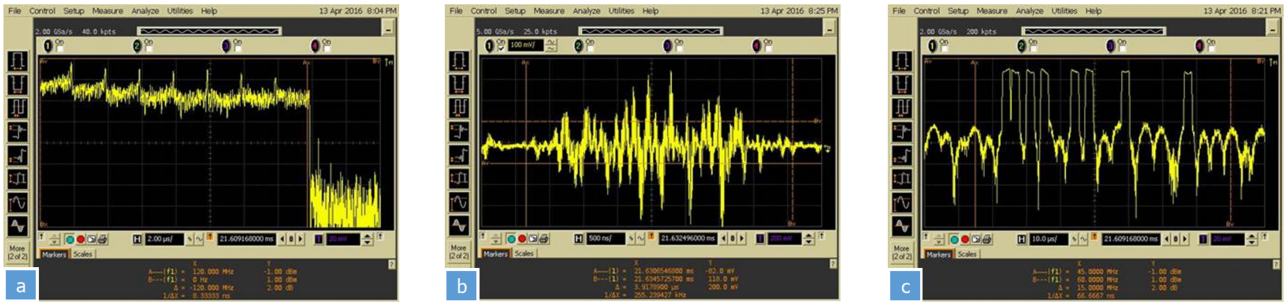
Fig. 7. Output of the waveform generator for one receive chain. (a) Spectrum over 120 MHz showing echoes from all 8 transmitters. (b) Single transmit waveform in time-domain. (c) Spectrum of single transmit signal showing that only eight 375 kHz slices out of available 12 MHz bandwidth are transmitted.

nels are fetched from memory. Each of the $\mathcal{I}$ and $\mathcal{Q}$ analog signals are then passed on to their respective APP cards. The waveform generator also produces timing signals such as system clock and triggers to indicate the beginning of each PRI. The latter is used by the digital receiver to begin the sampling operation when a new range-time profile is received.

Fig. 7(a) shows the output of the waveform generator for one receiver as seen on a spectrum analyzer. The echoes corresponding to all eight transmitters are present. Together, this signal is spread over 120 MHz. The time and frequency domain representations of a signal corresponding to a single Tx–Rx channel are provided in Fig. 7(b) and (c). Since the transmission is cognitive, the signal is restricted to only $N_b = 8$ narrow subbands, each of 375 kHz bandwidth. These cosets are chosen after extensive software simulations such that they provide low mutual coherence.

C. Analog Preprocessors

A custom-built APP (see Fig. 8) splits the 120 MHz baseband analog signal from the waveform generator into eight channels. The 9 dB attenuation due to an eight-channel Wilkinson splitter is compensated with the use of a 10 dB amplifier for each channel. The signal corresponding to each transmitter is then filtered using BPFs each with 12 MHz passband. We use two separate APP cards, for $\mathcal{I}$ and $\mathcal{Q}$ channels, mounted on the opposite sides of a single chassis (see Fig. 5).

We designed the analog filters for each Tx–Rx channel to obtain nearly 30 dB stop-band attenuation. As we explain below, our digital receiver subsamples the analog signal at 7.5 MHz while the Nyquist rate is 30 MHz. This yields a subsampling factor of $q = 4$. With these specifications, the stop-band attenuation of 30 dB (or $N_0/N_{\text{sub}} = 1000$, on linear scale) leads to an SNR_{loss} of only 0.035 dB, hugely mitigating the effect of out-band noise. All analog filters are elliptic because, for any given order, the elliptic filter gives a much higher rate of attenuation in the transition band. In our case, the guard band being 3 MHz, the filter response must reach stop-band attenuation of 30 dB at most 3 MHz away from the passband cutoff frequency. At the same time, the phase distortion or group delay in elliptic filters is the worst
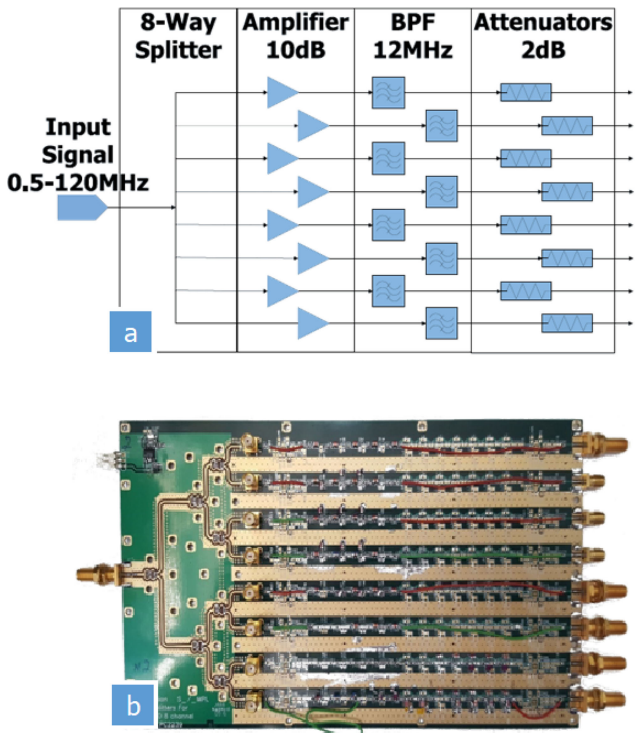

Fig. 8. (a) Block diagram of the APP chain. (b) APP card showing the baseband lumped circuit filters.

among standard responses such as Butterworth, Chebyshev, and Bessel filters [70]. We correct this distortion digitally in the receiver through extensive calibration of the entire analog chain.

Table III lists the specifications of all analog filters employed in the CoSUMMeR prototype. Only the first transmit channel uses a low-pass elliptic filter because it is difficult to practically realize a bandpass filter with a passband close to zero. The second and third channel filters are followed by tunable equalizers to correct the imbalance in gain. All other BPFs are realized by a combination of low- and high-pass elliptic filters with an overall passband ripple of 0.1 dB. Fig. 9 shows the theoretical magnitude and group delay response of each filter. Most of the responses achieve 30 dB attenuation in a transition band less than 3 MHz. Finally, as

TABLE III
Specifications of APP Filters

| Channel	Center Frequency	Passband	Type	Order	Passband Ripple (dB)	Stopband Attenuation	Equalizer
1	7 MHz	0-13.4 MHz	Low-pass elliptic	7	0.01	30dB@16MHz	No
2	22 MHz	16-28 MHz	Band-pass elliptic	5	0.4	30 dB @ 16 MHz 30 dB @ 31MHz	Yes
3	37 MHz	31-43 MHz	Band-pass elliptic	5	0.4	30 dB @ 28 MHz 30 dB @ 46 MHz	Yes
4	52 MHz	46.5-59.5 MHz	Low-pass & high-pass elliptic	9 (low-pass), 9 (high-pass)	0.1	30 dB @ 43 MHz 30 dB @ 61 MHz	No
5	67 MHz	61-73 MHz	Low-pass & high-pass elliptic	9 (low-pass), 9 (high-pass)	0.1	30 dB @ 58 MHz 30 dB @ 76 MHz	No
6	82 MHz	76-88 MHz	Low-pass & high-pass elliptic	9 (low-pass), 9 (high-pass)	0.1	30 dB @ 73 MHz 30 dB @ 91 MHz	No
7	97 MHz	91-103 MHz	Low-pass & high-pass elliptic	9 (low-pass), 9 (high-pass)	0.1	30 dB @ 88 MHz 30 dB @ 106 MHz	No
8	112 MHz	106-118 MHz	Low-pass & high-pass elliptic	9 (low-pass), 11 (high-pass)	0.1	30 dB @ 103 MHz 30 dB @ 121 MHz	No
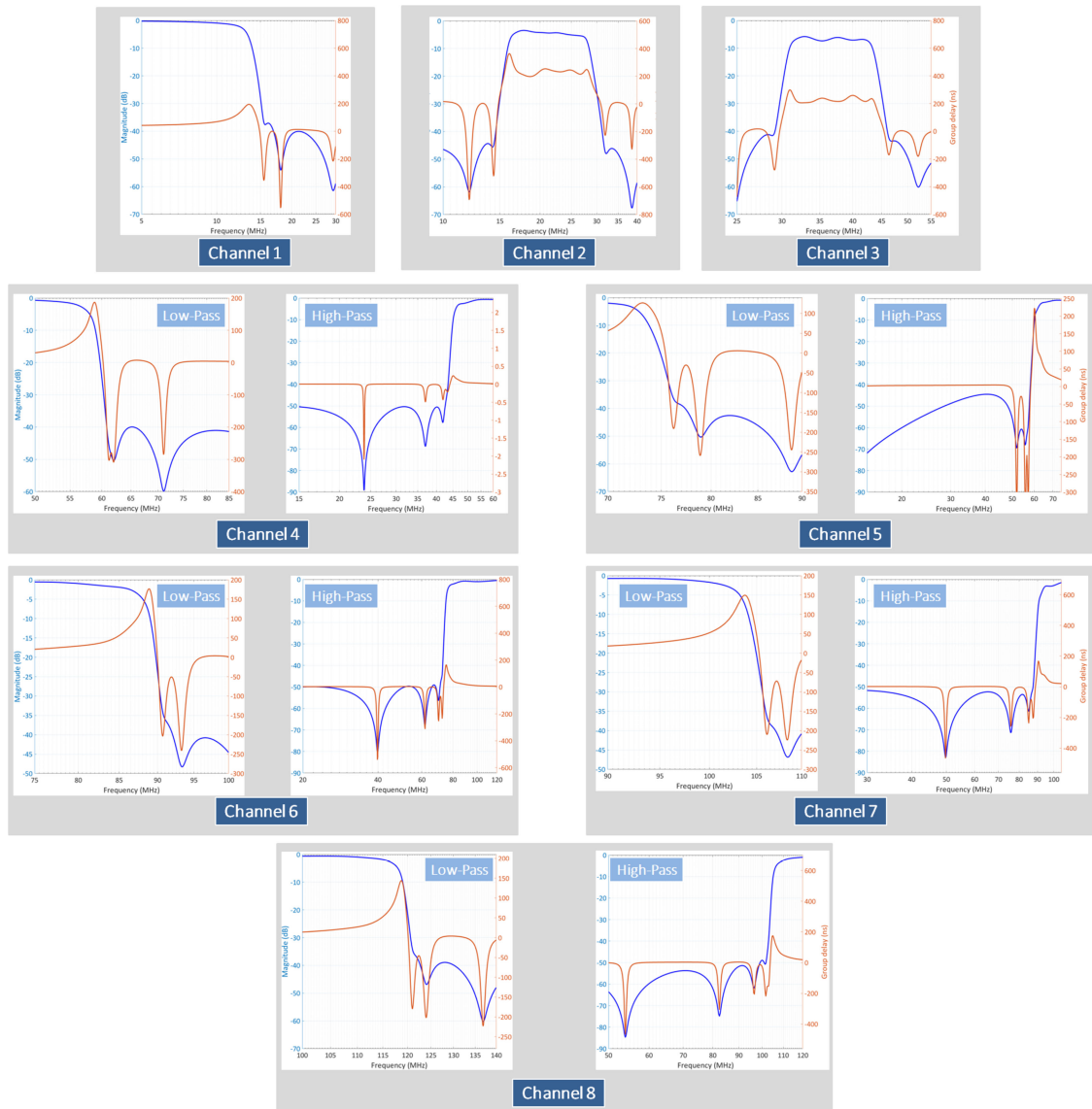
Fig. 9. Magnitude and group delay responses of analog filters. Filters for channels 4–8 are realized separately as low- and high-pass filters in the hardware.
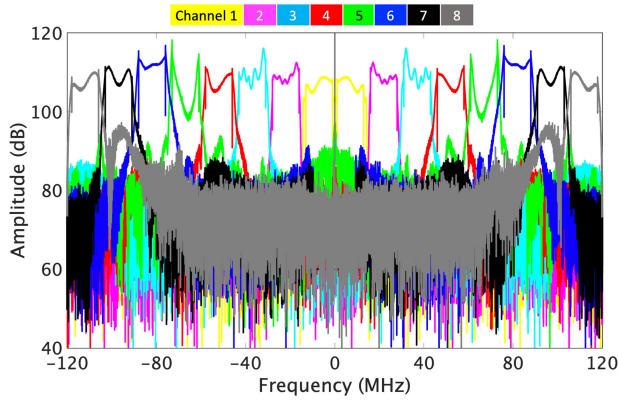
Fig. 10. Two-sided sampled magnitude response of all eight channels when the input is a BITE signal with an approximately flat spectrum across 120 MHz range.
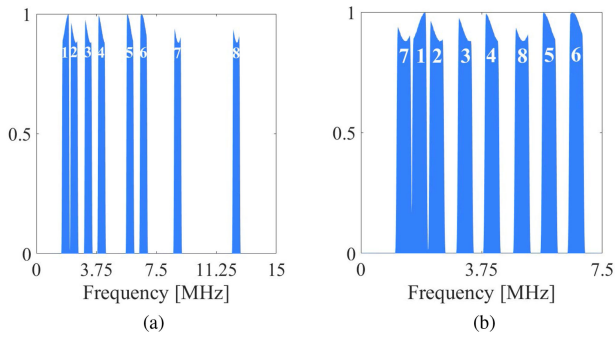

Fig. 11. Normalized one-sided spectrum of one channel of a given receiver (a) before and (b) after subsampling with a 7.5 MHz ADC. Each of the subbands span 375 kHz and is marked with a numeric label. In a noncognitive processing, the signal occupies the entire 15 MHz spectrum before sampling.

shown in Fig. 8(a), 2 dB attenuators are placed after each BPF in order to avoid saturating the digital receiver that follows APPs.

Fig. 10 shows the response of all eight filters as sampled by the digital receiver. The injected signal at the waveform generator was a standard BITE waveform (with flat spectrum over 120 MHz). We note that our design of analog filters is quite robust and provides excellent isolation of adjacent channels.

D. Digital Receivers

The digital receiver consists of a single Xilinx VC707 evaluation board with two eight-channel 4DSP FMC168 digitizer daughter cards, one each for $\mathcal{I}$ and $\mathcal{Q}$ signals. The channelized $\mathcal{I}/\mathcal{Q}$ analog signals are then digitized using low-rate 16-bit ADCs in a digital receiver card. As shown in Fig. 11(a), the cognitive radar signal occupies only certain subbands in a 15 MHz band of a single transmitter. Here, the sliced transmit signal has eight subbands each of width 375 kHz with frequency ranges 1.63–2, 2.16–2.53, 3.05–3.42, 3.88–4.25, 5.66–6.03, 6.51–6.88, 8.64–9.01, and 12.32–12.69 MHz before subsampling. The resulting coherence [17] for this selection of Fourier coefficients is 0.42. The total signal bandwidth is $0.375 \times 8 =$

3 MHz. This signal is subsampled at 7.5 MHz and, as shown in Fig. 11(b), there is no aliasing between different subbands.

The 4DSP FMC168 employs Texas Instruments ADS42LB69 ADC that has $E_{\text{NoB}} = 11.85$ and $P_{\text{sat}} = \pm 10$ dBm. This results in a dynamic range (in dB) of

$$\text{DR} = -1.76 + 6.02(11.85) + 10 \log_{10} \left(\frac{7.5/2}{1} \right) = 75.32 \tag{16}$$

with the lower limit of $\text{DR}_{\text{low}} = -10 - 75.32 = -85.32$ dBm, which is close to the digital noise floor of the receiver. This range is sufficient for us to experiment with various power levels during the cognitive mode. By default, we distribute power equally in all the subbands, which are of equal bandwidth, although other considerations such as presence of interference may also guide power allocation in practice [43].

The sampled data are transferred to an FPGA using 1.2 Gbps SerDes. The FPGA then writes the data to a digital first-in-first-out buffer from where an RJ-45 controller reads and transfers the signals to a data processor over the Ethernet link.

E. Data Processors and Radar Display

The data processor is a 64-bit Desktop server that receives the sampled data from the receiver and performs signal reconstruction by implementing the algorithm in [31] in real time. The number of Fourier coefficients corresponding to each transmitter bandwidth of 15 (or 12) MHz is 1500 while that for a single subband of 375 kHz bandwidth is 38. Therefore, the data processor uses a total of $8 \times 38 = 304$ Fourier coefficients during the reconstruction process.

The detection results of sub-Nyquist signal processing are shown on a radar display (see Fig. 5) in polar range-azimuth and Cartesian range-angle-Doppler plots. Here, individual channels can also be examined through their time-domain or A-scope plots. The display also stores the previous three results to allow comparison with the current configuration.

F. Resource Reduction

In Fig. 6, we overlay the spectra of Fig. 11 over the full bandwidth of the noncognitive signal before subsampling. A noncognitive signal occupies the entire 15 MHz spectrum requiring a Nyquist sampling rate of 30 MHz. On the other hand, our digital receiver samples at 7.5 MHz. Therefore, use of cognitive transmission enables temporal sampling reduction by a factor of 4 (= 30 MHz/7.5 MHz) for each channel. Depending on whether the guard bands of the noncognitive transmission are included in the computation or not, the effective signal bandwidth for each channel is reduced by a factor of 5 (= 15 MHz/3 MHz) or 4 (= 12 MHz/3 MHz), respectively. The sub-Nyquist array in Mode 3 employs only half the antenna elements than the Nyquist array in Mode 1. In other words, the spatial sampling rate in Mode 3 is reduced by 50% when

TABLE IV
CoSUMMeR Prototype: Comparison of Resource Reduction

Resource	Nyquist Mode 1	Sub-Nyquist Mode 3	Reduction	Nyquist 20×20 array	Sub-Nyquist Mode 4	Reduction
Bandwidth per Tx (including guard-bands)	15 MHz	3 MHz	80%	15 MHz	3 MHz	80%
Bandwidth per Tx (excluding guard-bands)	12 MHz	3 MHz	75%	12 MHz	3 MHz	75%
Temporal sampling rate per channel	30 MHz	7.5 MHz	75%	30 MHz	7.5 MHz	75%
Spatial sampling rate	8 × 10	4 × 5	50%	20 × 20	8 × 10	55%
Tx/Rx hardware channels	80	20	75%	400	80	80%
Total Tx bandwidth (including guard-bands)	120 MHz	12 MHz	90%	300 MHz	24 MHz	92%
Total Tx bandwidth (excluding guard-bands)	96 MHz	12 MHz	87.5%	240 MHz	24 MHz	90%

compared with Mode 1 or 2. If we account for both spatial and spectral sampling reduction in Mode 3, then we use a total one-eighth of the Nyquist sampling rate and one-tenth of the Nyquist signal bandwidth (guard bands included). The sampling rate reduction is, therefore, seven-eighth or 87.5% in Mode 3. In terms of the hardware cost, the receiver processes 80 and 20 Tx–Rx channels in 8 × 10 and 4 × 5 arrays, respectively. Thus, the hardware resources are reduced by 75% in Mode 3.

Similar comparisons of Mode 4 can be made with its Nyquist equivalent 20 × 20 array. Here, the reduction in temporal sampling rate and per transmitter bandwidth is the same as before. Since Mode 4 employs a total of 18 antenna elements compared to 40 of the virtual array, the sampling rate reduction is 55%. The corresponding savings in hardware due to reduction of Tx–Rx channels from 400 in the virtual array to 80 in Mode 4 is substantial (80%). The spatial sub-Nyquist rate reduction leads to a significantly low usage of transmit bandwidth in Mode 4. Table IV summarizes these comparisons.

In terms of system complexity, our design for 80 Tx–Rx channels is accomplished using 8 ADCs, 8 BPFs, and 8 analog channels. A noncognitive Nyquist design would require 80 units of each of these components. For a noncognitive sub-Nyquist design that serializes all receive data streams and employs subsampling, 88 BPFs—one for separating each of the Tx signals and another 8 to separate each of the subbands in 10 receivers—and 8 ADCs are required. If subsampling is forfeited, then serialization of receive data in a noncognitive sub-Nyquist design would consume 64 ADCs (one for each of the 8 subbands in 8 Tx) and 72 BPFs (64 each of the ADCs and 8 more to separate each Tx signal).

V. EXPERIMENTAL RESULTS

We evaluated the performance of CoSUMMeR through hardware experiments. The waveform generator produced $P = 10$ pulses at a PRI of 100 μs and we compared the signal reconstruction results of all modes for identical target scenarios. Cognitive transmission was operated at the near saturation level of the devices. While configuring the prototype for the noncognitive modes, we decreased the signal strength accordingly.

In the following, we present radar display outputs of three experiments. Here, a successful detection (circle with
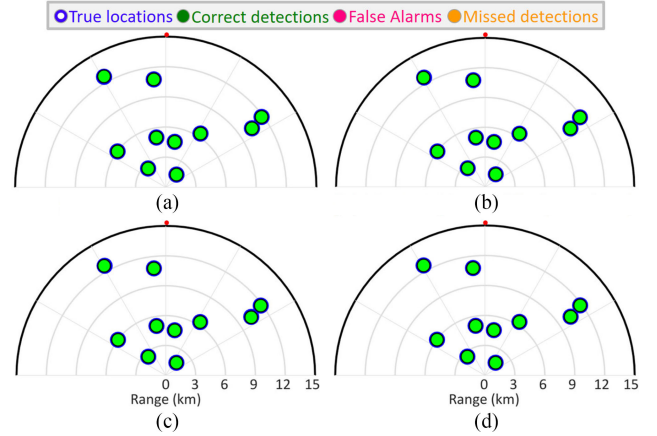

Fig. 12. PPI display of results for Modes 1 through 4. The origin is the location of the radar. The dark dot indicates the north direction relative to the radar. Positive (negative) distances along the horizontal axis correspond to the east (west) of the radar. Similarly, positive (negative) distances along the vertical axis correspond to the north (south) of the radar. The estimated targets are plotted over the ground truth. (a) Mode 1 (8 × 10 ULA). (b) Mode 2 (8 × 10 filled, random). (c) Mode 3 (4 × 5 thinned). (d) Mode 4 (8 × 10 thinned).

dark boundary and no fill) occurs when the estimated target is within one range cell, one azimuth bin and one Doppler bin of the ground truth (circle with light fill and no boundary); otherwise, the estimated target is labeled as a false alarm (circle with dark fill). Only for the purposes of clear illustration, we have magnified the circles; the exact location of the targets should be taken as the center of the circles.

Randomly spaced targets: In the first experiment, when the angular spacing (in terms of the sine of azimuth) between any two targets was greater than 0.025 and the signal SNR = −8 dB, the recovery performance of the thinned 4 × 5 array in Mode 3 was not worse than Modes 1 and 2. For this experiment, Figs. 12 and 13 show the plan position indicator (PPI) plot and range-azimuth-Doppler maps of all the modes, respectively. Successful detection in this case was *sensu stricto*, i.e., the estimated target was at the exact range-azimuth-Doppler bin of the ground truth.

Closely spaced targets: We next considered a sparse target scene with $L = 10$ targets including two pairs of targets closely spaced in azimuth, namely, with angular spacing of 0.02. The SNR of the injected signal was −5 dB. Since the angular resolution of Mode 4 is better than the
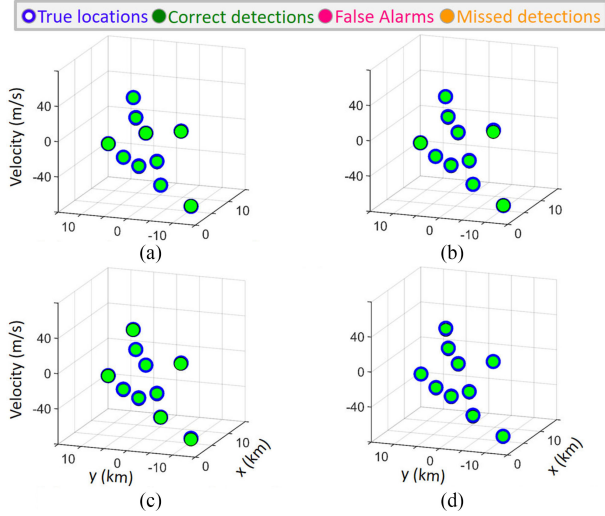
Fig. 13. Range-Azimuth-Doppler map for the target configurations shown in Fig. 12. The lower axes represent Cartesian coordinates of the polar representation of the PPI plots from Fig. 12. The vertical axis represents the Doppler spectrum. (a) Mode 1 (8×10 ULA). (b) Mode 2 (8×10 filled, random). (c) Mode 3 (4×5 thinned). (d) Mode 4 (8×10 thinned).

Fig. 15. Range-Azimuth-Doppler maps as in Fig. 13, but for a closely-spaced target scenario. The inset plots show the selected region in each map on a magnified scale. (a) Mode 1 (8×10 ULA). (b) Mode 2 (8×10 filled, random). (c) Mode 3 (4×5 thinned). (d) Mode 4 (8×10 thinned).
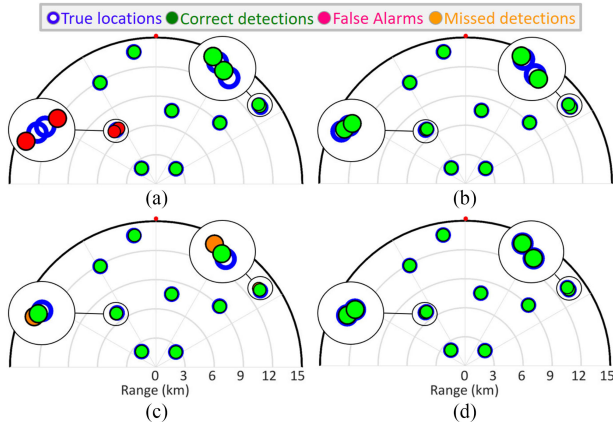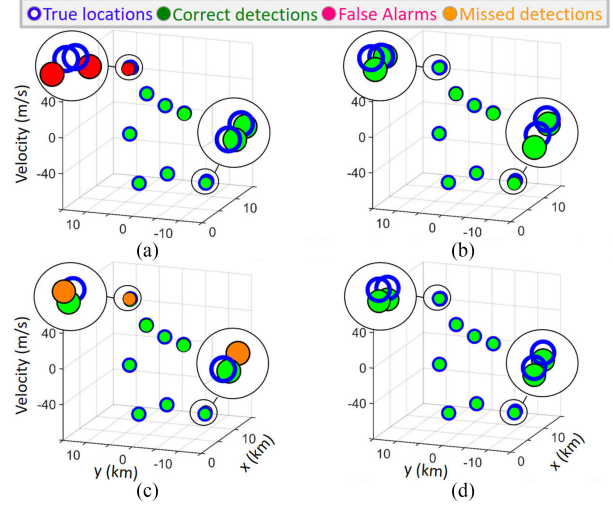

Fig. 14. PPI plots as in Fig. 12, but for a closely-spaced target scenario. The inset plots show the selected region in each PPI display on a magnified scale. (a) Mode 1 (8×10 ULA). (b) Mode 2 (8×10 filled, random). (c) Mode 3 (4×5 thinned). (d) Mode 4 (8×10 thinned).
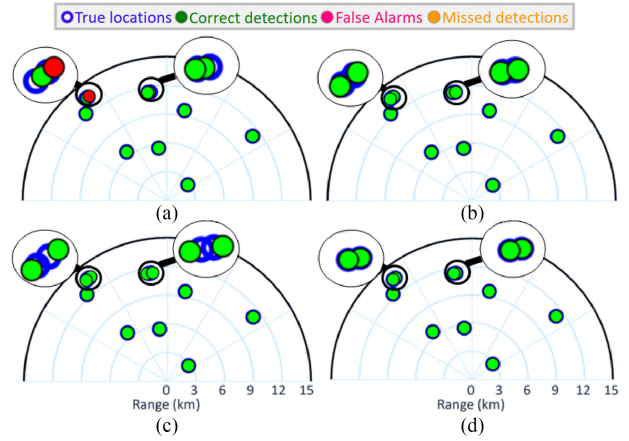

Fig. 16. PPI plots as in Fig. 12, but only Mode 3 is operating cognitively. All modes have the same overall transmit power per transmitter. The inset plots show the selected region in each PPI display on a magnified scale. (a) Mode 1 (8×10 ULA). (b) Mode 2 (8×10 filled, random). (c) Mode 3 (4×5 thinned). (d) Mode 4 (8×10 thinned).

other three modes, all the targets are successfully detected in Mode 4. Modes 1 and 3 produced a false alarm or missed detection as seen in the inset plots of Figs. 14 and 15. Mode 2 also shows successful recovery in the relaxed sense of our detection criterion. However, relatively better performance of Mode 2 over Modes 1 and 3 is not entirely fortuitous here. Fig. 4 shows that both Tx and Rx array elements in Mode 2 are distributed such that its virtual array is wider than Modes 1 and 3. Thus, the effective angular resolution for Mode 2 is better than 1 and 3, but still worse than 4.

Cognitive mode: We examined a high noise scenario with an injected signal SNR $= -15$ dB. We operated only Mode 3 cognitively (i.e., with increased subband power) and kept all other modes in noncognitive mode. We noticed that the noncognitive Nyquist 8×10 Mode 1 array

exhibits false alarms while cognitive sub-Nyquist 4×5 Mode 3 array is still able to detect all the targets (see Figs. 16 and 17), thereby demonstrating robustness to low SNR. As mentioned earlier, Modes 2 and 4 continue to yield successful detections due to their wide aperture. However, contrary to Mode 2, the detection in Mode 4 is *sensu stricto*.

Statistical performance: Finally, we evaluated the performance of the hardware prototype over 100 different trials each with a distinct randomly spaced $L = 10$ targets and $P = 10$ pulses. We fed the target echoes to the digital receiver in all four (noncognitive) modes as well as the cognitive Mode 3. Fig. 18 shows the occurrence (in percentage) of specific detection results for all five configurations. We note that, as SNR worsens, the performance of sub-Nyquist,
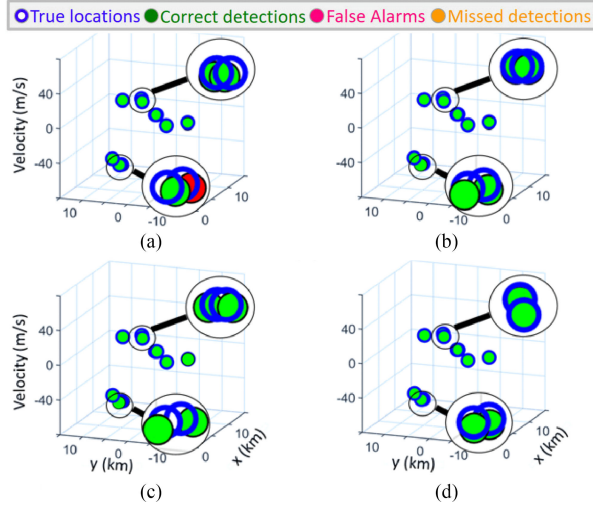
Fig. 17. Range-Azimuth-Doppler maps as in Fig. 13, but only Mode 3 is operating cognitively. All modes have the same overall transmit power per transmitter. The inset plots show the selected region in each map on a magnified scale. (a) Mode 1 (8×10 ULA). (b) Mode 2 (8×10 filled, random). (c) Mode 3 (4×5 thinned). (d) Mode 4 (8×10 thinned).

Fig. 18. Statistical performance of different array configurations in a CoSUMMeR prototype over 100 realizations of randomly spaced target scenes.

noncognitive Mode 3 worsens in comparison with Nyquist Mode 1. However, when Mode 3 operates cognitively, its probability of correct detection increases and is actually better than Mode 1.

VI. SUMMARY

We presented a hardware prototype of a cognitive, sub-Nyquist MIMO radar that demonstrates real-time operation of both spatial and temporal reduction in sampling leading to reduction in antenna elements and savings in signal bandwidth. The proposed thinned 4×5 array achieves the resolution and detection performance of its filled array counterpart even though the overall reduction in bandwidth is 87.5%. The hardware prototype is in-house and custom-made using many off-the-shelf components. The system operates in real time and its performance is robust to high noise.

We demonstrated that our sub-Nyquist MIMO receiver leads to the feasibility of cognitive MIMO radar (CoSUMMeR), which transmits thinned spectrum signals. This development is significant in enabling the spectral coexistence of MIMO radar with MIMO communications. Furthermore, CoSUMMeR improves sub-Nyquist processing performance in low-SNR situations by transmitting additional in-band power. We believe that such hardware implementations pave the way to identify further practical challenges in future deployment of sub-Nyquist radars.

REFERENCES

[1] E. Fishler, A. Haimovich, R. Blum, D. Chizhik, L. Cimini, and R. Valenzuela
     MIMO radar: An idea whose time has come
     In *Proc. IEEE Radar Conf.*, 2004, pp. 71–78.

[2] J. Li and P. Stoica
     MIMO radar with colocated antennas
     IEEE Signal Process. Mag., vol. 24, no. 5, pp. 106–114, Sep. 2007.

[3] I. Bekkerman and J. Tabrikian
     Target detection and localization using MIMO radars and sonars
     IEEE Trans. Signal Process., vol. 54, no. 10, pp. 3873–3883, Oct. 2006.

[4] R. Boyer
     Performance bounds and angular resolution limit for the moving colocated MIMO radar
     IEEE Trans. Signal Process., vol. 59, no. 4, pp. 1539–1552, Apr. 2011.

[5] M. Dianat, M. R. Taban, J. Dianat, and V. Sedighi
     Target localization using least squares estimation for MIMO radars with widely separated antennas
     IEEE Trans. Aerosp. Electron. Syst., vol. 49, no. 4, pp. 2730–2741, Oct. 2013.

[6] W. Huleihel, J. Tabrikian, and R. Shavit
     Optimal adaptive waveform design for cognitive MIMO radar
     IEEE Trans. Signal Process., vol. 61, no. 20, pp. 5075–5089, Oct. 2013.

[7] J. Xu, G. Liao, S. Zhu, L. Huang, and H. C. So
     Joint range and angle estimation using MIMO radar with frequency diverse array
     IEEE Trans. Signal Process., vol. 63, no. 13, pp. 3396–3410, Jul. 2015.

[8] A. M. Haimovich, R. S. Blum, and L. J. Cimini
MIMO radar with widely separated antennas
IEEE Signal Process. Mag., vol. 25, no. 1, pp. 116–129, Jan. 2008.

[9] Q. He, R. S. Blum, H. Godrich, and A. M. Haimovich
Target velocity estimation and antenna placement for MIMO radar with widely separated antennas
IEEE J. Sel. Topics Signal Process., vol. 4, no. 1, pp. 79–100, Feb. 2010.

[10] W. Khan, I. M. Qureshi, and K. Sultan
Ambiguity function of phased-MIMO radar with colocated antennas and its properties
IEEE Geosci. Remote Sens. Lett., vol. 11, no. 7, pp. 1220–1224, Jul. 2014.

[11] H. Godrich, A. M. Haimovich, and R. S. Blum
Target localization accuracy gain in MIMO radar-based systems
IEEE Trans. Inform. Theory, vol. 56, no. 6, pp. 2783–2803, Jun. 2010.

[12] Y. C. Eldar
Sampling Theory: Beyond Bandlimited Systems. Cambridge, U.K: Cambridge Univ. Press, 2015.

[13] E. Brookner
MIMO radar demystified and where it makes sense to use
In *Proc. IET Int. Radar Conf.*, 2014, pp. 1–6.

[14] J. H. Ender
On compressive sensing applied to radar
Signal Process., vol. 90, no. 5, pp. 1402–1414, 2010.

[15] K. V. Mishra and Y. C. Eldar
Sub-Nyquist radar: Principles and prototypes
in *Compressed Sensing in Radar Signal Processing*, A. D. Maio, Y. C. Eldar, and A. M. Haimovich, Eds. Cambridge University Press, 2019, in press.

[16] D. Cohen and Y. C. Eldar
Sub-Nyquist radar systems: Temporal, spectral and spatial compression
IEEE Signal Process. Mag., vol. 35, no. 6, pp. 35–58, Nov. 2018.

[17] Y. C. Eldar and G. Kutyniok
Compressed Sensing: Theory and Applications. Cambridge, U.K.: Cambridge Univ. Press, 2012.

[18] S. Gogineni and A. Nehorai
Target estimation using sparse modeling for distributed MIMO radar
IEEE Trans. Signal Process., vol. 59, no. 11, pp. 5315–5325, Nov. 2011.

[19] T. Strohmer and H. Wang
Sparse MIMO radar with random sensor arrays and Kerdock codes
In *Proc. IEEE Int. Conf. Sampling Theory Appl.*, 2013, pp. 517–520.

[20] T. Strohmer and B. Friedlander
Analysis of sparse MIMO radar
Appl. Comput. Harmonic Anal., vol. 37, no. 3, pp. 361–388, 2014.

[21] D. Malioutov, M. Cetin, and A. S. Willsky
A sparse signal reconstruction perspective for source localization with sensor arrays
IEEE Trans. Signal Process., vol. 53, no. 8, pp. 3010–3022, Aug. 2005.

[22] D. S. Kalogerias and A. P. Petropulu
Matrix completion in colocated MIMO radar: Recoverability, bounds & theoretical guarantees
IEEE Trans. Signal Process., vol. 62, no. 2, pp. 309–321, Jan. 2014.

[23] K. V. Mishra, A. Kruger, and W. F. Krajewski
Compressed sensing applied to weather radar
In *Proc. IEEE Int. Geosci. Remote Sens. Symp.*, 2014, pp. 1832–1835.

[24] S. Sun, W. U. Bajwa, and A. P. Petropulu
MIMO-MC radar: A MIMO radar approach based on matrix completion
IEEE Trans. Aerosp. Electron. Syst., vol. 51, no. 3, pp. 1839–1852, Jul. 2015.

[25] L. Carin
On the relationship between compressive sensing and random sensor arrays
IEEE Antennas Propag. Mag., vol. 51, no. 5, pp. 72–81, Oct. 2009.

[26] Y. Yu, A. P. Petropulu, and H. V. Poor
MIMO radar using compressive sampling
IEEE J. Sel. Topics Signal Process., vol. 4, no. 1, pp. 146–163, Feb. 2010.

[27] M. Rossi, A. M. Haimovich, and Y. C. Eldar
Spatial compressive sensing for MIMO radar
IEEE Trans. Signal Process., vol. 62, no. 2, pp. 419–430, Jan. 2014.

[28] K. V. Mishra, I. Kahane, A. Kaufmann, and Y. C. Eldar
High spatial resolution radar using thinned arrays
In *Proc. IEEE Radar Conf.*, 2017, pp. 1119–1124.

[29] S. Qin, Y. D. Zhang, and M. G. Amin
DoA estimation of mixed coherent and uncorrelated targets exploiting coprime MIMO radar
Digital Signal Process., vol. 61, pp. 26–34, 2017.

[30] E. Tohidi, M. Coutino, S. P. Chepuri, H. Behroozi, M. M. Nayebi, and G. Leus
Sparse antenna and pulse placement for colocated MIMO radar
IEEE Trans. Signal Process., vol. 67, no. 3, pp. 579–593, Feb. 2019.

[31] D. Cohen, D. Cohen, Y. C. Eldar, and A. M. Haimovich
SUMMeR: Sub-Nyquist MIMO radar
IEEE Trans. Signal Process., vol. 66, no. 16, pp. 4315–4330, Aug. 2018.

[32] E. Baransky, G. Itzhak, I. Shmuel, N. Wagner, E. Shoshan, and Y. C. Eldar
A sub-Nyquist radar prototype: Hardware and algorithms
IEEE Trans. Aerosp. Electron. Syst., vol. 50, no. 2, pp. 809–822, Apr. 2014.

[33] O. Bar-Ilan and Y. C. Eldar
Sub-Nyquist radar via Doppler focusing
IEEE Trans. Signal Process., vol. 62, no. 7, pp. 1796–1811, Apr. 2014.

[34] O. Rabaste, L. Savy, M. Cattenoz, and J.-P. Guyvarch
Signal waveforms and range/angle coupling in coherent colocated MIMO radar
In *Proc. IEEE Int. Conf. Radar*, 2013, pp. 157–162.

[35] D. Cohen, D. Cohen, and Y. C. Eldar
High resolution FDMA MIMO radar
2017, arXiv:1711.06560.

[36] K. V. Mishra *et al.*
Cognitive sub-Nyquist hardware prototype of a collocated MIMO radar
In *Proc. Int. Workshop Compressed Sens. Theory Appl. Radar, Sonar Remote Sens.*, 2016, pp. 56–60.

[37] D. Cohen *et al.*
Sub-Nyquist MIMO radar prototype with Doppler processing
In *Proc. IEEE Radar Conf.*, 2017, pp. 1179–1184.

[38] S. Haykin
Cognitive radar: A way of the future
IEEE Signal Process. Mag., vol. 23, no. 1, pp. 30–40, Jan. 2006.

[39] J. R. Guerci
Cognitive Radar: The Knowledge-Aided Fully Adaptive Approach. Norwood, MA, USA: Artech House, 2010.

[40] K. L. Bell, C. J. Baker, G. E. Smith, J. T. Johnson, and M. Rangaswamy
Cognitive radar framework for target detection and tracking

IEEE J. Sel. Topics Signal Process., vol. 9, no. 8, pp. 1427–1439, Dec. 2015.

[41] A. M. Elbir, K. V. Mishra, and Y. C. Eldar
Cognitive radar antenna selection via deep learning
IET Radar, Sonar Navigation, vol. 13, pp. 871–880, 2019.

[42] A. Aubry, A. De Maio, Y. Huang, M. Piezzo, and A. Farina
A new radar waveform design algorithm with improved feasibility for spectral coexistence
IEEE Trans. Aerosp. Electron. Syst., vol. 51, no. 2, pp. 1029–1038, Apr. 2015.

[43] K. V. Mishra and Y. C. Eldar
Performance of time delay estimation in a cognitive radar
In Proc. IEEE Int. Conf. Acoust., Speech Signal Process., 2017, pp. 3141–3145.

[44] D. Cohen, K. V. Mishra, and Y. C. Eldar
Spectrum sharing radar: Coexistence via Xampling
IEEE Trans. Aerosp. Electron. Syst., vol. 29, no. 3, pp. 1279–1296, Jun. 2018.

[45] K. V. Mishra, A. Zhitnikov, and Y. C. Eldar
Spectrum sharing solution for automotive radar
In Proc. IEEE Veh. Technol. Conf. - Spring, 2017, pp. 1–5.

[46] K. V. Mishra, M. R. Bhavani Shankar, V. Koivunen, B. Ottersten, and S. A. Vorobyov
Toward millimeter wave joint radar communications: A signal processing perspective
IEEE Signal Process. Mag., to be published, Sep. 2019.

[47] B. Li, A. P. Petropulu, and W. Trappe
Optimum co-design for spectrum sharing between matrix completion based MIMO radars and a MIMO communication system
IEEE Trans. Signal Process., vol. 64, no. 17, pp. 4562–4575, Sep. 2016.

[48] F. Liu, C. Masouros, A. Li, H. Sun, and L. Hanzo
MU-MIMO communications with MIMO radar: From co-existence to joint transmission
IEEE Trans. Wireless Commun., vol. 17, no. 4, pp. 2755–2770, Apr. 2018.

[49] J. Qian, M. Lops, L. Zheng, X. Wang, and Z. He
Joint system design for coexistence of MIMO radar and MIMO communication
IEEE Trans. Signal Process., vol. 66, no. 13, pp. 3504–3519, Jul. 2018.

[50] S. Na, K. V. Mishra, Y. Liu, Y. C. Eldar, and X. Wang
TenDSuR: Tensor-based 3D sub-Nyquist radar
IEEE Signal Process. Lett., vol. 26, no. 2, pp. 237–241, Feb. 2019.

[51] K. V. Mishra and Y. C. Eldar
Sub-Nyquist channel estimation over IEEE 802.11ad link
In Proc. IEEE Int. Conf. Sampling Theory Appl., 2017, pp. 355–359.

[52] Y. C. Eldar, R. Levi, and A. Cohen
Clutter removal in sub-Nyquist radar
IEEE Signal Process. Lett., vol. 22, no. 2, pp. 177–181, Feb. 2015.

[53] D. Cohen, A. Dikopoltsev, R. Ifraimov, and Y. C. Eldar
Towards sub-Nyquist cognitive radar
In Proc. IEEE Radar Conf., 2016, pp. 1–5.

[54] K. M. Cohen, C. Attias, B. Farbman, I. Tselniker, and Y. C. Eldar
Channel estimation in UWB channels using compressed sensing
In Proc. IEEE Int. Conf. Acoust., Speech Signal Process., 2014, pp. 1966–1970.

[55] C. Ma, T. S. Yeo, C. S. Tan, and Z. Liu
Three-dimensional imaging of targets using colocated MIMO radar
IEEE Trans. Geosci. Remote Sens., vol. 49, no. 8, pp. 3009–3021, Aug. 2011.

[56] W.-Q. Wang
MIMO SAR imaging: Potential and challenges
IEEE Aerosp. Electron. Syst. Mag., vol. 28, no. 8, pp. 18–23, Aug. 2013.

[57] C. Ma, T. S. Yeo, C. S. Tan, J.-Y. Li, and Y. Shang
Three-dimensional imaging using colocated MIMO radar and ISAR technique
IEEE Trans. Geosci. Remote Sens., vol. 50, no. 8, pp. 3189–3201, Aug. 2012.

[58] X. Zhuge and A. G. Yarovoy
A sparse aperture MIMO-SAR-based UWB imaging system for concealed weapon detection
IEEE Trans. Geosci. Remote Sens., vol. 49, no. 1, pp. 509–518, Jan. 2011.

[59] J. Klare and O. Saalmann
MIRA-CLE X: A new imaging MIMO-radar for multi-purpose applications
In Proc. Eur. Radar Conf., 2010, pp. 129–132.

[60] T. Rommel, A. Patyuchenko, P. Laskowski, M. Younis, and G. Krieger
An orthogonal waveform scheme for imaging MIMO-Radar applications
In Proc. Int. Radar Symp., 2013, vol. 2, pp. 917–922.

[61] F. Belfiori, N. Maas, P. Hoogeboom, and W. van Rossum
TDMA X-band FMCW MIMO radar for short range surveillance applications
In Proc. Eur. Conf. Antennas Propag., 2011, pp. 483–487.

[62] O. Biallawons, J. Klare, and O. Saalmann
Technical realization of the MIMO radar MIRA-CLE Ka
In Proc. Eur. Radar Conf., 2013, pp. 21–24.

[63] R. Feger, C. Wagner, S. Schuster, S. Scheiblhofer, H. Jager, and A. Stelzer
A 77-GHz FMCW MIMO radar based on an SiGe single-chip transceiver
IEEE Trans. Microw. Theory Techn., vol. 57, no. 5, pp. 1020–1035, May 2009.

[64] A. Pedross-Engel, C. M. Watts, D. R. Smith, and M. S. Reynolds
Enhanced resolution stripmap mode using dynamic metasurface antennas
IEEE Trans. Geosci. Remote Sens., vol. 55, no. 7, pp. 3764–3772, Jul. 2017.

[65] T. Fromenteze, M. Boyarsky, J. Gollub, T. Sleasman, M. Imani, and D. R. Smith
Single-frequency near-field MIMO imaging
In Proc. Eur. Conf. Antennas Propag., 2017, pp. 1415–1418.

[66] M. I. Skolnik
Radar Handbook, 3rd ed. New York, NY, USA: McGraw-Hill, 2008.

[67] M. Mishali and Y. C. Eldar
From theory to practice: Sub-Nyquist sampling of sparse wideband analog signals
IEEE J. Sel. Topics Signal Process., vol. 4, no. 2, pp. 375–391, Apr. 2010.

[68] K. V. Mishra, V. Chandrasekar, C. Nguyen, and M. Vega
The signal processor system for the NASA dual-frequency dual-polarized Doppler radar
In Proc. IEEE Int. Geosci. Remote Sens. Symp., 2012, pp. 4774–4777.

[69] K. V. Mishra
Frequency diversity wideband digital receiver and signal processor for solid-state dual-polarimetric weather radars
Master's thesis, Colorado State Univ., Fort Collins, CO, USA, 2012.

[70] M. E. Van Valkenburg
Analog Filter Design. Holt, New York, NY, USA: Rinehart and Winston, 1982.

Kumar Vijay Mishra (S'08–M'15–SM'18) received the B. Tech. degree (*summa cum laude,* gold medal, honors), in electronics and communications engineering from the National Institute of Technology, Hamirpur, India, in 2003, the M.S. degree in electrical and computer engineering from Colorado State University, Fort Collins, CO, USA, in 2012, and the M.S. degree in mathematics and the Ph.D. degree in electrical and computer engineering from The University of Iowa, Iowa City, IA, USA, in 2015.

He is currently a visiting scholar with The University of Iowa, Iowa City, IA, USA, and technical advisor to the automotive radar startup Hertzwell, Singapore. His research interests include radar systems (theory and hardware), signal processing, remote sensing, and electromagnetics.

Dr. Mishra has more than 15 years of experience in research and development of various radar systems. From 2003 to 2007, he worked on military surveillance radars as a research scientist at the Electronics and Radar Development Establishment (LRDE), Defense Research and Development Organization (DRDO), Bengaluru. He was a research intern at Mitsubishi Electric Research Labs (Cambridge) and at Qualcomm (San Jose) in 2015. From 2015 to 2017, he was Andrew and Erna Finci Viterbi and Lady Davis Postdoctoral Fellow at the Viterbi Faculty of Electrical Engineering, Technion-Israel Institute of Technology. He is the recipient of Royal Meteorological Society Quarterly Journal Editor's Prize (2017), Lady Davis Fellowship (2016/2017), Andrew and Erna Finci Viterbi Fellowship (twice awarded, 2015 and 2016), Technion EE Excellent Undergraduate Adviser Award (2017), Cornell Base-of-Pyramid Narrative Competition Prize (2009), Altera Forum Guru Challenge Winner (2008), DRDO LRDE Scientist of the Year Award (2006), NITH Directors Gold Medals for 1st rank in the Department of Electronics and Communication Engineering and entire university during the undergraduate commencement (2003), and NITH Best Student Award (2003).

Yonina C. Eldar (S'98–M'02–SM'07–F'12) received the B.Sc. degree in physics and the B.Sc. degree in electrical engineering both from Tel-Aviv University (TAU), Tel-Aviv, Israel, in 1995 and 1996, respectively, and the Ph.D. degree in electrical engineering and computer science from the Massachusetts Institute of Technology (MIT), Cambridge, MA, USA, in 2002.

From January 2002 to July 2002, she was a Postdoctoral Fellow with the Digital Signal Processing Group with MIT. She is currently a Professor with the Department of Mathematics and Computer Science, Weizmann Institute of Science, Rehovot, Israel. She was previously a Professor with the Department of Electrical Engineering, the Technion, where she held the Edwards Chair in Engineering. She is also a Visiting Professor with MIT, a Visiting Scientist at the Broad Institute, and an Adjunct Professor at Duke University and was a Visiting Professor at Stanford. She is the author of the book *Sampling Theory: Beyond Bandlimited Systems* and coauthor of the books *Compressed Sensing* and *Convex Optimization Methods in Signal Processing and Communications*, all published by Cambridge University Press.

Dr. Eldar has received numerous awards for excellence in research and teaching, including the IEEE Signal Processing Society Technical Achievement Award (2013), the IEEE/AESS Fred Nathanson Memorial Radar Award (2014), and the IEEE Kiyo Tomiyasu Award (2016). She was a Horev Fellow of the Leaders in Science and Technology program at the Technion and an Alon Fellow. She received the Michael Bruno Memorial Award from the Rothschild Foundation, the Weizmann Prize for Exact Sciences, the Wolf Foundation Krill Prize for Excellence in Scientific Research, the Henry Taub Prize for Excellence in Research (twice), the Hershel Rich Innovation Award (three times), the Award for Women with Distinguished Contributions, the Andre and Bella Meyer Lectureship, the Career Development Chair at the Technion, the Muriel & David Jacknow Award for Excellence in Teaching, and the Technions Award for Excellence in Teaching (twice). She received several best paper awards and best demo awards together with her research students and colleagues including the SIAM outstanding Paper Prize and the IET Circuits, Devices and Systems Premium Award, and was selected as one of the 50 most influential women in Israel.She is a member of the Israel Academy of Sciences and Humanities (elected 2017), a EURASIP Fellow. She was a member of the Young Israel Academy of Science and

Humanities and the Israel Committee for Higher Education. She is the Editor-in-Chief of Foundations and Trends in Signal Processing, a member of the IEEE Sensor Array and Multichannel Technical Committee and serves on several other IEEE committees. In the past, she was a Signal Processing Society Distinguished Lecturer, member of the IEEE Signal Processing Theory and Methods and Bio Imaging Signal Processing technical committees, and served as an Associate Editor for the IEEE TRANSACTIONS ON SIGNAL PROCESSING, the *EURASIP Journal of Signal Processing*, the *SIAM Journal on Matrix Analysis and Applications*, and the *SIAM Journal on Imaging Sciences*. She was Co-Chair and Technical Co-Chair of several international conferences and workshops.

Eli Shoshan, photograph and biography not available at the time of publication.

Moshe Namer, photograph and biography not available at the time of publication.

Maxim Meltsin, photograph and biography not available at the time of publication.